TUDelft

Delft University of Technology

Benchmarking analytical and numerical simulation of induced fault slip

Novikov, A. V.; Shokrollahzadeh Behbahani, S.; Voskov, D.; Hajibeygi, H.; Jansen, J. D.

Important note
To cite this publication, please use the final published version (if applicable).
Please check the document version above.

Benchmarking analytical and numerical simulation of induced fault slip

Novikov, A.V. and Shokrollahzadeh Behbahani, S.

Voskov, D., Hajibeygi, H. and Jansen, J.D.

Department of Geoscience and Engineering, TU Delft, Delft, Netherlands

ABSTRACT: Quantification of the poromechanical response of subsurface formations due to human-induced pore pressure fluctuations is critical for the performance and stability assessment of many geo-energy systems. In particular, natural faults in the subsurface introduce the hazard of induced seismicity. Numerical modeling of fault reactivation is challenging, while the specific details of induced stresses and fault slip in reservoirs with displaced (i.e. non-zero offset) faults may cause additional challenges depending on the type of numerical formulation employed. To facilitate the systematic development and testing of numerical tools for the simulation of induced seismicity in faulted reservoirs we developed a set of semi-analytical test problems of increasing complexity, based on inclusion theory and Cauchy singular integral equations. With these we investigate the accuracy of two recently developed Finite Volume (FV) schemes with collocated and staggered arrangements of unknowns. One of them employs a conformal discrete fault model (DFM) which can guarantee sufficient accuracy at the cost of adaptive mesh refinement but may suffer from modelling and computational challenges when addressing large-scale realistic geological configurations. The second one employs an embedded (or non-conformal) discrete fault model (EDFM) which avoids the need for excessive mesh refinement, but of which the accuracy and the range of applicability are still to be investigated. We found that both numerical schemes accurately represent the pre-slip Coulomb stresses, but show different degrees of accuracy in representing the resulting depletion-induced fault slip. The semi-analytical benchmark data are available via DOI 10.4121/22240309.

1 INTRODUCTION

The kernel of this paper is formed by a series of semi-analytical poro-mechanical test problems of increasing complexity with the aim to systematically compare the capacities of two poro-mechanical finite-volume-based simulation codes: one developed by Novikov et al. (2022b) which employs a discrete fault model (DFM). It forms part of a comprehensive porous media simulation package, the Delft Advanced Reservoir Terra Simulator (DARTS) and will be referred to with that acronym. The second code, developed by Shokrollahzadeh Behbahani et al. (2022), is based on a smoothed version of the embedded discrete fault model (sEFVM) and will be referred to with that last acronym. Both codes are being developed as part of the *DeepNL Science4Steer* project (NWO, 2017), and Appendices A and B give a brief overview of their characteristic features. The grids used in this study are presented in Appendix C.

The comparison is performed against semi-analytical solutions of pre-slip stress fields and the resulting induced fault slip, developed using inclusion theory and Cauchy singular integral equations with details reported earlier in Jansen et al. (2019) and Jansen and Meulenbroek (2022). Appendix D gives a brief overview of these methods. The semi-analytical benchmark data used to generate the figures in this paper are available in the form of an Excel file uploaded to the 4TU Data Repository with DOI 10.4121/22240309.

We employ the solids mechanics sign convention, i.e. positive strains and stresses imply extension and tension respectively. Pore pressures are taken as positive. We will frequently refer to *inital* and *incremental* variables. The former refer to the situation before the start of reservoir

depletion and are indicated with lower case letters with superscript 0. The latter refer to the situation during reservoir depletion and are indicated with plain lower case letters. The sums of initial and incremental variables will be referred to as *combined* variables and they are indicated with capitals. In particular, we have

$$\Sigma = \sigma^0 + \sigma, \tag{1}$$

$$P = p^0 + p, \tag{2}$$

to indicate combined stresses and pressures respectively. As regards the stresses, we will apply the common notation for *total* stresses σ and *effective* stresses σ' which are related to each other according to

$$\sigma' = \sigma + \alpha p, \tag{3}$$

$$\sigma'^0 = \sigma^0 + \alpha p^0, \tag{4}$$

$$\Sigma' = \Sigma + \alpha P, \tag{5}$$

where α is the Biot coefficient (Wang, 2000).

2 DEPLETION IN A RESERVOIR WITHOUT FAULTS

2.1. Model

Consider a schematic representation of a simulation domain to model a homogeneous horizontal reservoir with part of the overburden and underburden and without faults; see Fig. 1. The simulation domain forms a square with the vertically centered reservoir covering the entire width and with the origin of the coordinate system in the middle. As a first step, we consider quasi-steady-state poro-mechanics in a domain with uniform elastic properties. In that case, there is no need to solve for the pressure field which, instead, can be specified in each cell a priori. Moreover, it is assumed that no incremental pressure change will occur in the overburden and underburden. The incremental reservoir pressure, as occurs during depletion, can therefore be simulated by specifying the pressure in the reservoir cells while keeping the pressures in the overburden and underburden equal to their initial values. (Alternatively, these burdens may be represented as consisting of a purely elastic solid without porosity.)

Fig. 1 indicates the horizontal and vertical load configuration and the mechanical boundary conditions to simulate the initial stress field. The dimensions of the simulation domain and the reservoir are indicated in Table 1, with $a = b = 112.5$ m, together with several other parameters that will be of relevance for later steps of the code comparison exercise. Uniform vertical distributed loads, with different magnitudes and opposite directions, are applied from the top and bottom boundaries, while non-uniform
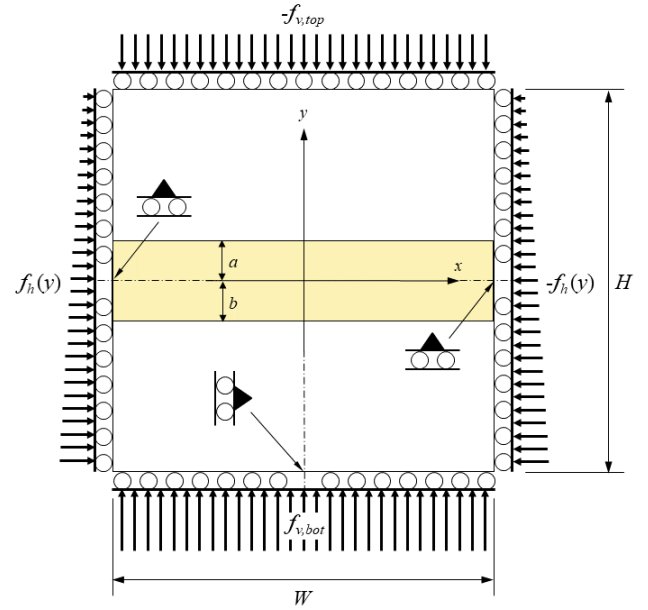

Fig. 1: Simulation set-up to represent an infinitely wide reservoir without faults (not to scale). Load configuration and mechanical boundary conditions to simulate initial stresses.

horizontal distributed loads, with equal magnitudes but opposite directions, are applied from both sides, thus ensuring a stress field that is symmetric around the y axis. To constrain rigid body translations and rotation, horizontal displacement is constrained at a single point at the bottom center while vertical displacements are constrained in single points at the left and right boundaries. In all other points at the boundaries, the shear stresses are set equal to zero, as indicated by the 'rollers' at all sides. This configuration, with a minimum number of constraints at the boundaries, ensures that during the initial loading no spurious shear stresses are developed because of restricted displacements. Further details of the initial stress field are given in the next section. After simulation of these initial stresses, all vertical displacements are shifted such that the reference (zero vertical displacement) is located at the bottom of the simulation domain.

To enable the subsequent simulation of depletion, the vertical boundary conditions are changed to roller-type ones with fixed horizontal displacements, and the bottom one to a roller-type condition with fixed vertical displacements; see Fig. 2. The three constraints at the bottom and the sides are removed. Together with the use of plane-strain conditions in the simulation codes, which can be interpreted as fixing the horizontal displacements in z direction, and given the horizontally constant geometry of the reservoir layer, the simulation domain now approximates an infinite horizontal reservoir in x and z directions.

Table 1: Reservoir properties, fault geometry and simulation domain.

Symbol	Property	Value	SI units
a	See Figs.	112.5 or 75	m
b	"	112.5 or 150	m
D_0	Depth at reservoir center ($y = 0$)	3500	m
g	Acceleration of gravity	9.81	m/s^2
G	Shear modulus	6500	MPa
H	Height of simulation domain	4500	m
K^0	Ratio of initial effective horizontal to vertical stresses	0.5	–
p	Incremental reservoir pressure	−25	MPa
p_0^0	Initial reservoir pressure at reservoir center	35	MPa
W	Width of simulation domain	4500	m
α	Biot coefficient	0.9	–
β	Effective stress coefficient for fault friction	0.9	–
θ	Dip angle	90 or 70	deg.
κ	Cohesion	0	MPa
μ	friction coefficient	0.52	–
ν	Poisson's coefficient	0.15	–
ρ_{fl}	Fluid density	1020	kg/m^3
ρ_s	Solid density	2650	kg/m^3
ϕ	Porosity	0.15	–

Note: the initial vertical stress, initial pressure and initial effective normal stress have been computed as:
$$\sigma_{yy}^0(y) = [(1-\phi)\rho_s + \phi\rho_{fl}]g(y - D_0), \text{ where } \sigma_v^0 < 0,$$
$$p^0(y) = p_0^0 - \rho_{fl}\,g\,y,$$
$$\sigma_{\perp}'^0(y) = \sigma_{\perp}^0(y) + \alpha p^0(y).$$
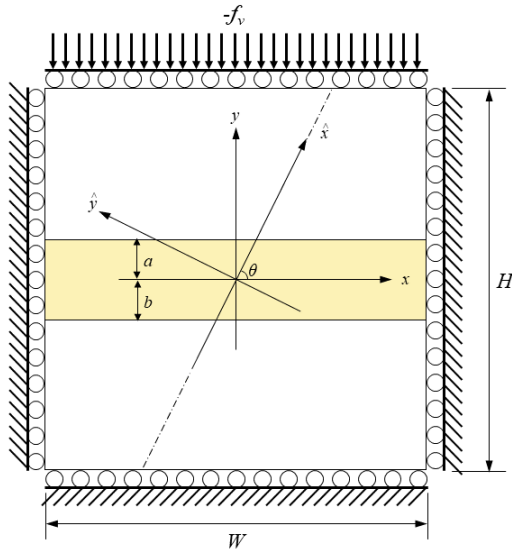(Valid for reservoir, overburden and underburden.)

Fig. 2: Identical to Fig. 1 but now with load configuration and mechanical boundary conditions to simulate incremental stresses. The figure also shows a line through the center at an angle of $\theta = 70$ degrees with respect to horizontal, with an associated rotated $\hat{x} - \hat{y}$ coordinate system.

2.2. Initial stresses

With the center of the reservoir (and therefore the center of the simulation domain) at a depth of 3500 m and a height of the simulation domain of 4500 m it follows that the top of the domain is at 1250 m below surface and 2250 m above the center. The required vertical distributed load $f_{v,top}$ to simulate the combined rock and fluid weight of the overburden at that depth follows from the text at the bottom of Table 1 as

$$
\begin{aligned}
f_{v,top} &= \sigma_{yy}^0(2250) \\
&= [(1-\phi)\rho_s + \phi\rho_{fl}]g(y - D_0) \\
&= -29.50e6 \text{ Pa},
\end{aligned}
\tag{6}
$$

where ϕ is porosity, ρ_s is solid density, ρ_{fl} is fluid density, g is acceleration of gravity, and D_0 is depth below surface at the vertical center of the reservoir. Because compressive normal stresses are negative, $f_{v,top}$ is also negative valued which implies that it acts in the negative y direction (i.e. downward, as indicated in Fig. 1.) The distributed load at the bottom of the domain is obtained in the same manner as

$$f_{v,bot} = -\sigma_{yy}^0(-2250) = 135.7e6 \text{ Pa}, \tag{7}$$

which, in line with its positive value, acts upward. The required horizontal distributed load f_h can be obtained as

$$
\begin{aligned}
f_h(y) &= -\sigma_{xx}^0(y) \\
&= -\left\{ K^0[\sigma_{yy}^0(y) + \alpha p^0(y)] - \alpha p^0(y) \right\}, \quad (8)
\end{aligned}
$$

where K^0 is the ratio of initial effective horizontal to vertical stresses. Because the initial fluid pressures at the top and bottom of the simulation domain are given by

$$
p^0(2250) = p_0^0 - \rho_{fl}\, g\, y = 12.49e6 \text{ Pa}, \quad (9)
$$
$$
p^0(-2250) = 57.51e6 \text{ Pa}, \quad (10)
$$

where p_0^0 is the initial reservoir pressure at depth D_0, the values of f_h at the top and bottom of the domain follow as

$$
f_h(2250) = 20.37e6 \text{ Pa}, \quad (11)
$$
$$
f_h(-2250) = 93.73e6 \text{ Pa}, \quad (12)
$$

where the positive values of f_h imply that they act in the positive x direction, i.e. to the right, as indicated at the left boundary in Fig. 1. A distributed load $-f_h$, with identical magnitude but acting in the negative x direction, is applied at the right boundary. The corresponding initial stress and pressure fields are given by

$$
\sigma_{xx}^0(y) = -57.05e6 + 16.30e3 \times y \text{ Pa}, \quad (13)
$$
$$
\sigma_{yy}^0(y) = -82.60e6 + 23.60e3 \times y \text{ Pa}, \quad (14)
$$
$$
p^0(y) = 35.00e6 - 10.06e3 \times y \text{ Pa}. \quad (15)
$$

Note that the initial shear stresses σ_{xy}^0 are zero by design.

2.3. Incremental stresses

After computation of the initial stresses, removal of the three constrained displacements, and fixing of horizontal displacements at the vertical boundaries and vertical displacements at the bottom, depletion can be simulated by adding a (negative) incremental pressure p to the cells in the reservoir. As indicated in Table 1, the standard depletion in our series of examples is $-25e6$ Pa.

2.4. Results

The application of distributed loads $f_{v,top}$, $f_{v,bot}$ and $\pm f_h$ to the boundaries, in order to compute the initial stress field, leads to initial vertical and horizontal displacements $u_y^0(x,y)$ and $u_x^0(x,y)$. We can use the constitutive equations for poro-elastic plane strain to approximately compute $u_y^0(y)$, i.e. independent of x, at the top boundary (Wang, 2000, Eq. 7.3). Assuming that the reference level of zero vertical displacements has been relocated to the bottom of the simulation domain (at $y = -2250$ m) this

results in

$$
\begin{aligned}
u_y^0(2250) &= \int_{-\frac{H}{2}}^{\frac{H}{2}} \epsilon_{yy}^0\, dy \\
&= \frac{1}{E} \int_{-\frac{H}{2}}^{\frac{H}{2}} (1-v^2)\sigma_{yy}^0(y) - v(1+v)\sigma_{xx}^0(y) \\
&\qquad + \alpha(1+v)(1-2v)p^0(y)\, dy \\
&= -13.66 \text{ m}, \quad (16)
\end{aligned}
$$

where H is the height of the simulation domain and E is Young's modulus which is computed from the shear modulus G and Poisson's ratio v as $E = 2G(1+v) = 15.0e9$ Pa. The approximate initial horizontal displacements at the top left and bottom left of the simulation domain follow as (Wang, 2000, Eq. 7.2)

$$
\begin{aligned}
u_x^0(-2250, 2250) &= -\int_{-\frac{W}{2}}^{0} \epsilon_{xx}^0(2250)\, dx \\
&= -\frac{W}{2}\epsilon_{xx}^0(2250) = 0.87 \text{ m}, \quad (17)
\end{aligned}
$$
$$
u_x^0(-2250, -2250) = 3.98 \text{ m}, \quad (18)
$$

where we used

$$
\begin{aligned}
\epsilon_{xx}^0(y) = -\frac{W}{2E}[&(1-v^2)\sigma_{xx}^0(y) - v(1+v)\sigma_{yy}^0(y) \\
&+ \alpha(1+v)(1-2v)p^0(y)], \quad (19)
\end{aligned}
$$

and where W is the width of the simulation domain. Identical displacements, but in opposite direction occur at the right boundary. The true displacement field will show small deviations from these approximate values because of contraction effects due to non-isotropic compression of the simulation domain as a result of the nonuniform initial distributed loads. However, the initial displacement field is not relevant for the subsequent steps in the comparison, as opposed to the initial stress field which is important because it determines the initial Coulomb stresses at the faults which will be considered later on.

As a reference for a future inclined fault configuration, consider a line through the center at an angle $\theta = 70$ deg. with respect to horizontal; see Fig. 2. The normal and shear stresses along this line can be computed as (Jansen and Meulenbroek, 2022, Eqs. 2 and 3)

$$
\begin{aligned}
\sigma_\perp^0(y) &= \sigma_{\hat{y}\hat{y}}^0(y) \\
&= \sigma_{xx}^0(y)\sin^2\theta + \sigma_{yy}^0(y)\cos^2\theta \\
&= -60.04e6 + 17.15e3 \times y \text{ Pa}, \quad (20) \\
\sigma_\parallel^0(y) &= -\sigma_{\hat{x}\hat{y}}^0(y) \\
&= (\sigma_{xx}^0(y) - \sigma_{yy}^0(y))\sin\theta\cos\theta \\
&= 8.21e6 - 2.35e3 \times y \text{ Pa}, \quad (21)
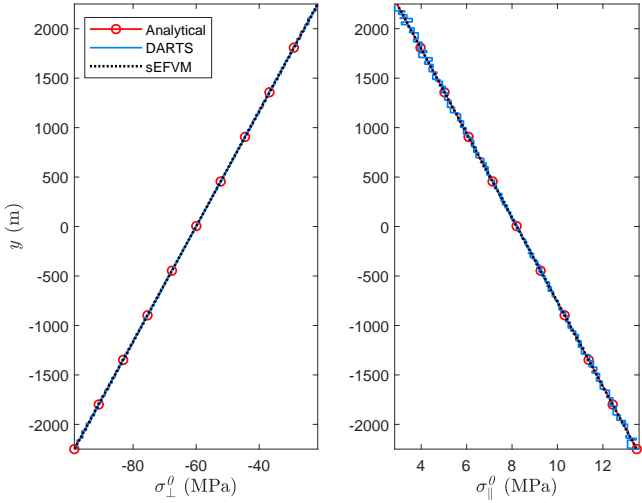\end{aligned}
$$

Fig. 3: Initial normal stresses (left) and initial shear stresses (right) along a line through the center of the reservoir at an angle of 70 deg. with horizontal.
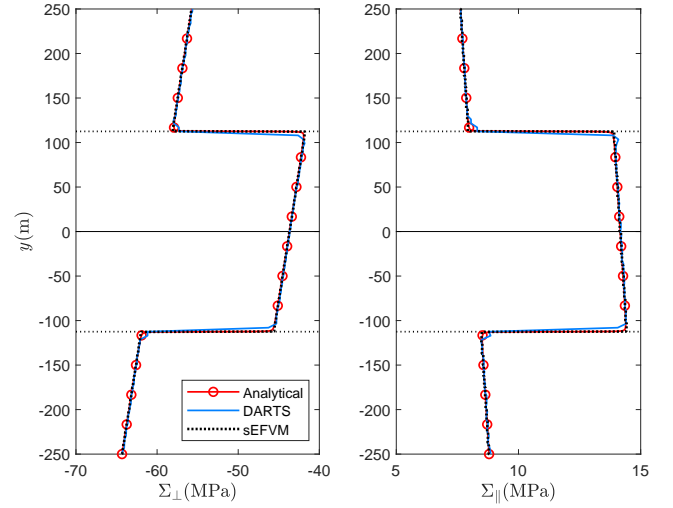

Fig. 4: Combined normal stresses (left) and combined shear stresses (right) along a line through the center of the reservoir at an angle of 70 deg. with horizontal.

where $\hat{x}$ and $\hat{y}$ are co-rotated coordinates. The sign convention of the shear stresses $\sigma_\parallel$ has been chosen such that positive shear stresses indicate a normal faulting tendency, i.e. tendency for the right block to shift upward with respect to the left block.

Fig. 3 displays the initial normal stresses and shear stresses along the inclined line for the two simulation codes and the analytical solution. Both codes produce a fully satisfactory match although the DARTS results for the shear stresses display small irregularities resulting from the use of an unstructured grid.

After changing the boundary conditions to fix the initial stress field, reservoir depletion will result in a uniform vertical compression. The combined vertical total stress Σ_{yy} will remain equal to the initial vertical total stress σ_{yy}^0 because the weight of the overburden remains the same (no arching occurs). The incremental vertical total stress σ_{yy} will therefore be zero and the incremental pressure will result in an incremental effective vertical stress with magnitude $\sigma_{yy}' = \alpha p$. The uniaxial vertical stiffness is given by the uniaxial compaction modulus (Wang, 2000, Eq. 6.5)

$$K_v = 2G\frac{1-\nu}{1-2\nu} = 15.79e9 \text{ Pa}, \qquad (22)$$

such that with a depletion of $-25e6$ Pa we expect a reservoir compaction, i.e. a negative change Δh of the reservoir height h (where $h = a + b$; see Fig. 1), according to

$$\Delta h = h\epsilon_{yy} = h\frac{\sigma_{yy}'}{K_v} = h\frac{\alpha p}{K_v} = -0.32 \text{ m.} \qquad (23)$$

The incremental horizontal strain ϵ_{xx} remains equal to

zero, because of the infinite horizontal extent of the reservoir, while the incremental horizontal effective stress is equal to (Wang, 2000, Eq. 6.4)

$$\sigma_{xx}' = \frac{\nu}{1-\nu}\sigma_{yy}' = \frac{\nu}{1-\nu}\alpha p = -3.97e6 \text{ Pa}, \qquad (24)$$

such that the incremental total horizontal stress becomes

$$\sigma_{xx} = \sigma_{xx}' - \alpha p = 18.53e6 \text{ Pa.} \qquad (25)$$

For this simple case of a reservoir without faults no incremental shear stresses σ_{xy} develop, and because there were no initial shear stresses σ_{xy}^0 it follows that also the combined shear stresses Σ_{xy} vanish. However, for the line at an angle $\theta = 70$ deg. that was considered earlier in Fig. 3, the incremental horizontal stresses σ_{xx} have an effect on both the incremental normal and shear stresses $\sigma_\perp$ and $\sigma_\parallel$, and therefore also on the combined normal and shear stresses $\Sigma_\perp$ and $\Sigma_\parallel$.

Fig. 4 displays the near-reservoir details of $\Sigma_\perp$ and $\Sigma_\parallel$ along the inclined line for the two simulation codes and the analytical solution. Both codes produce a fully satisfactory match. We note that DARTS demonstrates a somewhat higher relative accuracy for normal stresses than for shear, especially in Fig. 3, a feature that is explained by the higher magnitude of the normal stress.

3 DEPLETION IN A RESERVOIR WITH A VERTICAL FAULT WITH OFFSET AND NO FRICTION

Consider the same reservoir as before while introducing a displaced vertical fault at the center of the reservoir by
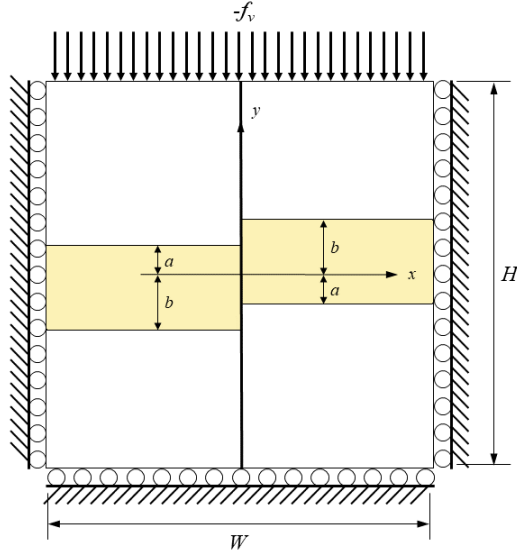
Fig. 5: Simulation set-up for a reservoir with a vertical displaced fault (not to scale).
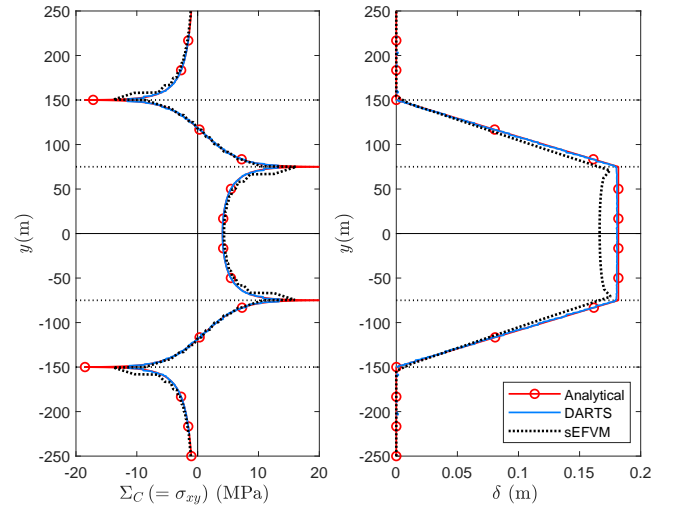

Fig. 6: Left: pre-slip Coulomb stresses Σ_C in a frictionless vertical fault with offset (which, for this particular case, just equals the incremental shear stress $\sigma_{\parallel}$). Right: the resulting slip δ.

choosing $a = 75\,\text{m}$ and $b = 150\,\text{m}$ such that the reservoir has the same height $h = a + b = 225\,\text{m}$ as before but now contains a fault with throw $t_f = b - a = 75\,\text{m}$; see Fig. 5. As a first step, we don't allow for fault slip in the simulation and perform the same steps as in the previous example to generate the initial and incremental stress fields.

The combined pre-slip Coulomb stress Σ_C, i.e. the pre-slip Coulomb stress resulting from the sum of initial and incremental stresses is defined for an arbitrarily oriented fault with friction coefficient μ as

$$\Sigma_C = |\Sigma_{\parallel}| + \mu \Sigma_{\perp}. \qquad (26)$$

For the particular case of a positive shear stress in a vertical fault without friction, i.e. with $\theta = 90$ degrees and $\mu = 0$, and an incremental pressure of $p = -25$ MPa this reduces to (Jansen and Meulenbroek, 2022, Eqs. 8 and 9)

$$\Sigma_C = -\sigma_{\hat{x}\hat{y}} = \sigma_{xy} = \frac{C}{2} \ln \frac{(y-a)^2 (y+a)^2}{(y-b)^2 (y+b)^2}, \qquad (27)$$

where C is given by

$$C = \frac{(1-2\nu)\alpha p}{2\pi(1-\nu)} = -2.95e6\,\text{Pa}. \qquad (28)$$

Next, we allow for slip in the fault over the entire simulation domain, i.e. from -2250 to 2250 m. The pressure in the fault is equal to the initial pressure $p^0(y)$ except for the reservoir section $-150\,\text{m} \geq y \geq 150\,\text{m}$ where it is equal to the combined pressure $P = p^0(y) - 25e6$ Pa. The analytical solution for the fault slip is given by (Jansen and

Meulenbroek, 2022, Eqs. (25) and (35))

$$\delta(y) = \frac{C}{A} \times \begin{cases} 0 & \text{if} & y \leq -b, \\ -(y+b) & \text{if} & -b < y \leq -a, \\ (a-b) & \text{if} & -a < y < a, \\ (y-b) & \text{if} & a \leq y < b, \\ 0 & \text{if} & b \leq y \ , \end{cases} \qquad (29)$$

where

$$A = \frac{G}{2\pi(1-\nu)} = 1.2171e09\,\text{Pa}, \qquad (30)$$

such that we obtain

$$\delta(y) = -0.0024$$
$$\times \begin{cases} 0 & \text{if} & y \leq -150, \\ -(y+150) & \text{if} & -150 < y \leq -75, \\ (75-150) & \text{if} & -75 < y < 75, \\ (y-150) & \text{if} & 75 \leq y < 150, \\ 0 & \text{if} & 150 \leq y \ , \end{cases} \qquad (31)$$

with all distances expressed in meters. Fig. 6 (right) displays this slip distribution over the height of the reservoir, and Fig. 6 (left) displays the pre-slip Coulomb stress.

The correspondence between the DARTS results and the semi-analytical results is excellent. The sEFVM results are slightly in error. This is because sEFVM calculates the slip by enriching the displacement field with one additional degree of freedom per matrix grid node. This is as opposed to other embedded methods such as XFEM, where in 2D each node that is enriched with the jump function is given 2 degrees of freedom. For fault tip enrichment, there are 4 extra degrees of freedom. This means
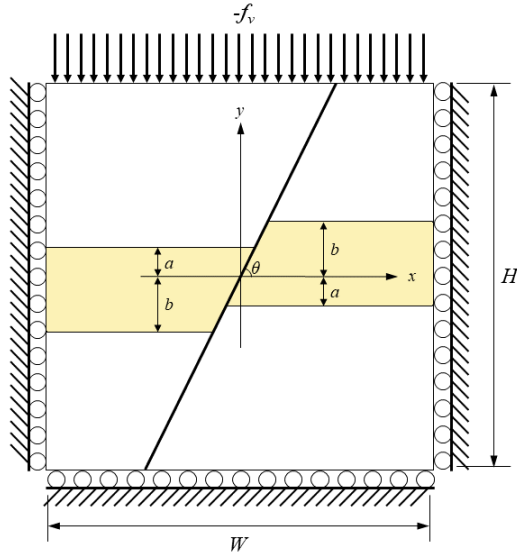
Fig. 7: Simulation set-up for a reservoir with an inclined displaced fault (not to scale).

Fig. 8: Left: pre-slip shear stresses $\Sigma_\parallel$ and slip threshold Σ_{sl} in an inclined fault with offset and constant friction. Right: the corresponding pre-slip Coulomb stresses Σ_C. Simulation domain width $W = 4500$ m.

sEFVM is much faster in terms of CPU time, but the predictions are expected to be less accurate Li et al. (2020); Xu et al. (2021).

4 DEPLETION IN A RESERVOIR WITH AN INCLINED FAULT WITH OFFSET AND CONSTANT FRICTION

Consider the same reservoir as in the previous step but now with a normal fault at 70 deg. with respect to horizontal; see Fig. 7. Fig. 8 (left) displays the pre-slip shear stresses $\Sigma_\parallel$ and the slip threshold $\Sigma_{sl} = -\mu\Sigma'_\perp$ for an incremental pressure $p = -25$ MPa, and Fig. 8 (right) shows the corresponding pre-slip Coulomb stresses.

Again, the DARTS results closely resemble the semi-analytical ones, while the sEFVM results display small deviations, especially near the stress peaks at $y = \pm75$ m and $y = \pm150$ m. As shown in Fig. 13, sEFVM uses a Cartesian grid with embedded faults to model the system. As a consequence, oscillations in the stress profiles can arise when the fault is misaligned with the grid. A smoothing step in sEFVM addresses these oscillations for improved estimation of slip. However, this smoothing also flattens the kinks at $y = \pm75$ m and $y = \pm150$ m.

Fig. 9 displays the post-slip Coulomb stresses (left) and fault slip (right) for $p = -25$ MPa. At this depletion level the slip occurs in the form of two separate slip patches. For increasing depletion, the patches will merge as shown in the same figure with results for $p = -27$ MPa. Somewhat surprisingly the DARTS results now show a discrepancy with the semi-analytical ones, especially for the merged
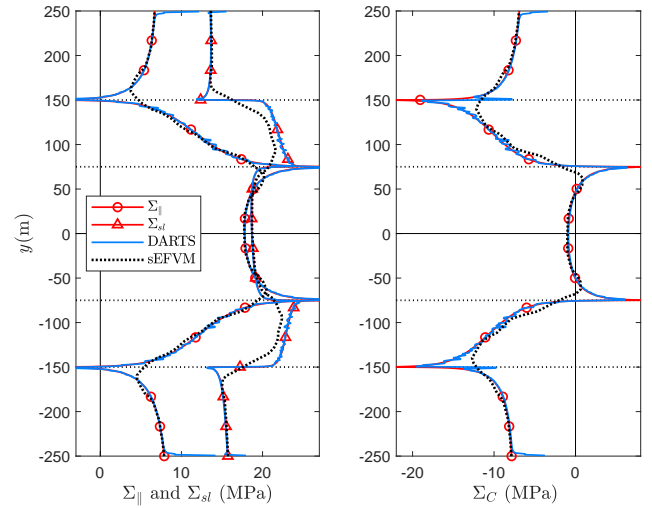
slip patch. Further comparisons revealed that this discrepancy disappears if the width W of the simulation domain is increased. Fig. 10 displays the same results but now for a simulation with $W = 18000$ m, i.e. four times as wide as the original simulation domain. Apparently, the strongly nonlinear mechanics involved in fault slip leads to strong sensitivities of the slip patch size to the boundary conditions at the edges of the reservoir. (This finding suggests that in reality there will also be a large sensitivity to the boundary conditions of the reservoir and probably also a significant interaction effect of neighboring faults.) Fig. 11 displays the reservoir and the simulation domain, with increased width, to scale.

Fig. 12 displays the location of the four slip patch boundaries (two for each of the two patches) as a function of incremental pressure. Merging occurs when the pressure has dropped to $p = -26.9$ MPa and the DARTS results (computed with $W = 18000$ m) match the semi-analytical ones. The sFEVM results for Figs. 9 to 12 did not fully converge for these test cases and displayed some unexpected features which require further research.
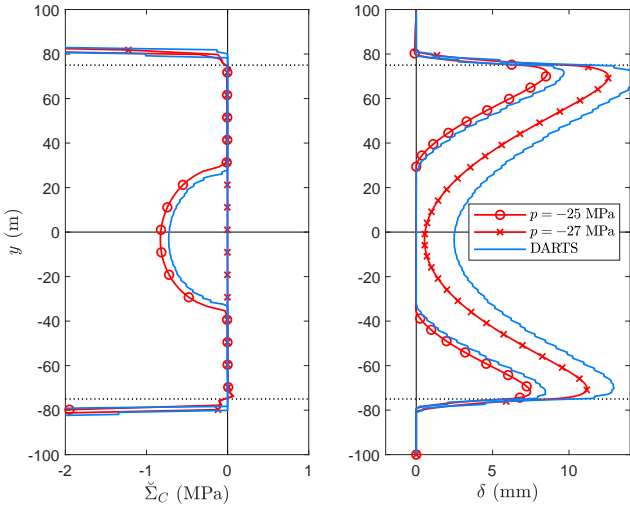
Fig. 9: Left: post-slip Coulomb stresses $\check{\Sigma}_C$. Right: the corresponding slip δ. Simulation domain width $W = 4500$ m.

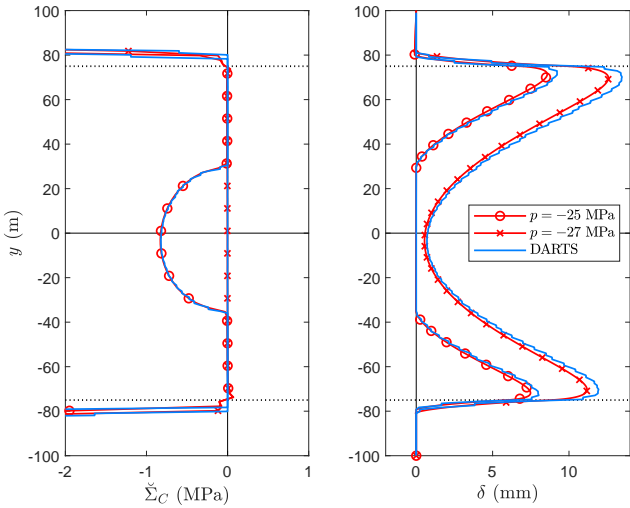
Fig. 10: Left: post-slip Coulomb stresses $\check{\Sigma}_C$. Right: the corresponding slip δ. Simulation domain width $W = 18000$ m.
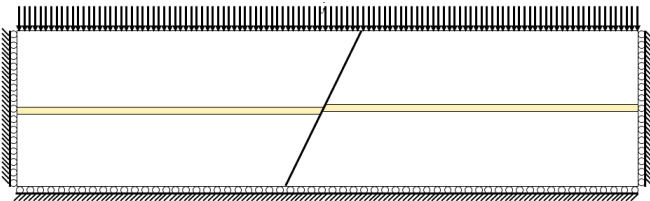

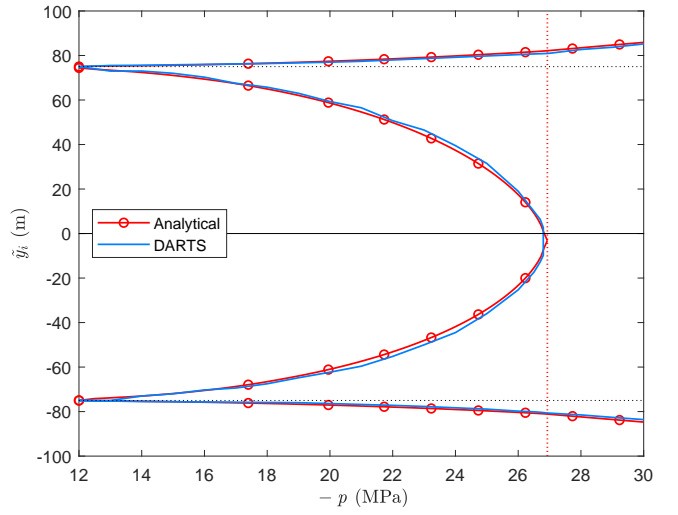Fig. 11: Simulation set-up, with increased width $W = 18000$ m, to scale.

Fig. 12: Slip patch boundaries as a function of depletion pressure p. The vertical dotted line indicates the merging pressure. Simulation domain width $W = 18000$ m.

APPENDIX A. COLLOCATED FVM WITH DFM

The system of single-phase fluid mass balance and static momentum balance equations for porous media can be written as

$$-\nabla \cdot \Sigma = (\phi \rho_f + (1-\phi)\rho_s)g\nabla y, \tag{32}$$

$$\frac{\partial}{\partial t}\left(\phi \rho_f\right) - \nabla \cdot \left(\frac{\rho_f K}{\mu_f}\left(\nabla p - \rho_f g\nabla y\right)\right) = r, \tag{33}$$

subjected to the constitutive relations (Coussy, 2004)

$$\Sigma = \boldsymbol{C} : \nabla^s (u - u_0) - pB, \tag{34}$$

$$\phi = \phi_0 + \frac{\text{tr}(B)/3 - \phi_0}{K_r}(p - p_0) + B : \nabla^s u, \tag{35}$$

where Σ is a rank-two total stress tensor, ϕ is porosity, ρ_{fl}, ρ_s are fluid and matrix densities, p is pore pressure, g is accelleration of gravity, y is depth, K is a rank-two permeability tensor, μ_f is fluid viscosity, r is a source of mass, $\boldsymbol{C}$ is a rank-four drained stiffness tensor for the rock matrix, ∇^s is the symmetric gradient operator, u is a vector of displacements, B is a rank-two tensor of Biot coefficients, subscript "0" denotes the initial value of a variable, $\text{tr}(B)$ is the trace of B, and K_r is the bulk modulus of the solid phase. Eqs. (32), (33) are subject to corresponding boundary and initial conditions.

At the fault interfaces, we consider a gap vector g that is equal to the jump of displacements over the contact $g = u^+ - u^-$, where the + asd − signs denote a particular side of the fault. The contact conditions following Simo and

Laursen (1992) read

$$g_N \leq 0, \tag{36}$$

$$f'_T - \mu f'_N \frac{\dot{g}_T}{|\dot{g}_T|} = 0, \quad \Phi = 0, \quad |\dot{g}_T| \neq 0, \quad \text{(slip)}, \tag{37}$$

$$\dot{g}_T = 0, \quad \Phi < 0, \quad \text{(stick)}, \tag{38}$$

where $f = -\Sigma \cdot n$ is the total traction vector, $f' = -(\Sigma + pB) \cdot n$ is the effective (Biot) traction vector, $f'_N = n^T f'$ and $f'_T = (I - nn^T) f'$ are the scalar normal and vectorial tangential projections of f' on the fault; g_N and g_T are the equivalent normal and tangential projections of g on the fault; $\dot{g}$ stands for the time derivative of the gap vector and $\Phi = |f'_T| - \mu f'_N$ is the Coulomb friction function with μ the friction coefficient. Eq. (36) represents a non-penetration condition, Eq. (37) governs relaxation of tangential traction once slip occurs, and Eq. (38) sets the change of the tangential gap (i.e. the slip) to zero if the slip criterion is not exceeded.

In the case of a collocated arrangement of unknown displacements and pore pressure, we can formulate discrete balance equations in a unified way. We use the cell-centered Finite Volume Method (FVM) to discretize Eqs. (32) and (33) (Novikov et al., 2022b,a). They can be written in cell i in the following vector form

$$V_i \begin{pmatrix} \Delta t \rho_{t,i}^{n+1} g \nabla y \\ (\tilde{\phi} \rho_f)|_{i,n}^{i,n+1} + \Delta t r_i^{n+1} \end{pmatrix} + $$
$$+ \sum_{j \in \partial V_i} \delta_{ij} \begin{pmatrix} \Delta t f_{ij}^{n+1} \\ \rho_{fi} \tilde{q}_{f,ij}|_n^{n+1} + \Delta t (\rho_f q_f / \mu_f)_{ij}^{n+1} \end{pmatrix} = 0, \tag{39}$$

where subscript j denotes the neighbours of cell i, Δt is the time step size, V_i is the volume of cell i, δ_{ij} denotes the area of the connection between cells i and j, superscripts n, and $n+1$ denote the variables taken from the current and next time step, respectively, while $\tilde{\phi}$ and $\tilde{q}_{ij}$ are defined as

$$\tilde{\phi} = \phi_0 + \frac{\text{tr}(B)/3 - \phi_0}{K_s}(p - p_0), \tag{40}$$

$$\tilde{q}_{f,ij} = (u - u_0)|_i^{ij} \cdot (Bn)_{ij}, \tag{41}$$

where last term is approximated using Gauss' formula as a sum of fluxes $\tilde{q}_{f,ij}$ over cell interfaces. The term $(\rho_f / \mu_f)_{ij}$ is calculated using an upwind approximation.

We use a gradient-based coupled multi-point stress and multi-point flux approximation for $f_{ij}, q_{f,ij}$ and $\tilde{q}_{f,ij}$ (Novikov et al., 2022b,a).

To satisfy Eqs. (36)-(38), we use a penalty regularization (Simo and Laursen, 1992; Yastrebov, 2013) which leads

to a return-mapping algorithm according to

$$f_N^{'n+1} - \varepsilon_N \langle g_N^{n+1} \rangle = 0, \tag{42}$$

$$\tilde{f}'_T = f_T^{'n} + \varepsilon_T (g_T^{n+1} - g_T^n), \quad \widetilde{\Phi} = \left| \tilde{f}'_T \right| - \mu^{n+1} f_N^{'n+1}, \tag{43}$$

$$f_T^{'n+1} - \tilde{f}'_T + \langle \widetilde{\Phi} \rangle \frac{\tilde{f}'_T}{\left| \tilde{f}'_T \right|} = 0, \tag{44}$$

where $\tilde{f}'_T$ denotes a trial traction, which represents the penalized effective tangential traction (Simo and Laursen, 1992). Penalty parameters $\varepsilon_N, \varepsilon_T \gg 1$ are calculated as $\varepsilon_N = f_{scale} E \delta / V, \varepsilon_T = f_{scale} G \delta / V$ where f_{scale} is an empirical scaling factor, δ denotes the area of contact interface, V stands for the mean volume of two neighbouring matrix cells, while E and G denote the mean Young's and shear moduli of two neighbouring matrix cells (Cardiff et al., 2017). Moreover, the Coulomb friction function Φ used as a slipping criterion is evaluated at the trial state $\widetilde{\Phi} = \Phi(\tilde{f}')$ that accounts for the change of slip g_T over the time step. Macaulay brackets are used to indicate that $\langle a \rangle$ is equal to a if $a \geq 0$ and otherwise equal to zero. Thus, in the slip state $\widetilde{\Phi} = 0$ Eq. (44) requires contact to remain at the slipping surface defined by $\Phi = 0$ where the direction of forces is defined by the trial traction. Contact reaches the stick state once the slip increment in Eq. (43) becomes negligible compared to the previous traction ($\dot{g}_T = \mathbf{0}$). In this case, Eq. (44) claims the traction to be equal to the trial one. In our experience, the return-mapping algorithm described in Eqs. (43)-(44) does not exhibit significant convergence problems, except for cases with severe inf-sup instability (pressure oscillations) and when the slip direction reverses. We may also expect convergence issues in the presence of intersecting faults or in the case of a hydraulically active fault when its volume and transmissibilities depend on the aperture g_N.

Note that we treat displacements over the lower-dimensional fault interface as discontinuous whereas pressure remains continuous there according to the assumptions of the equidimensional DFM approach. Sometimes this combination is called the mixed-dimensional fault model (Boon and Nordbotten, 2022).

APPENDIX B. SMOOTHED ENHANCED FINITE VOLUME METHOD

The smooth enhanced finite volume method (sEFVM) (Shokrollahzadeh Behbahani et al., 2022) uses the finite volume method (FVM) for both mechanics and flow. The mass conservation equations for a single phase, slightly-compressible flow inside a poroelastic domain with conductive faults using the embedded discrete fracture modeling (EDFM) method read (Hajibeygi et al., 2011; Li et al.,

2008),

$$\alpha \frac{\partial \nabla \cdot \vec{u}}{\partial t} + \frac{1}{M} \frac{\partial p_m}{\partial t} + \nabla \cdot \left(-\frac{K_f}{\mu_f} \cdot \nabla p_m \right) + \Psi_{m \to f} = Q_m, \tag{45}$$

and

$$\frac{\partial E_f}{\partial t} + \nabla \cdot \left(-\frac{aK_f}{\mu_f} \cdot \nabla p_f \right) + \Psi_{f \to m} = Q_f, \tag{46}$$

where p is pressure, t is time, M is the Biot modulus, Ψ is the net flux between the fault and matrix and a is aperture of the fault. E^f is the fault accumulation which is negligible if fault porosity is constant (McClure and Horne, 2011). Subscripts f and m indicate the fault and matrix, respectively.

The linear momentum balance for a faulted poroelastic medium can be expressed as

$$\nabla \cdot (\widetilde{\sigma} - \alpha p \widetilde{I}) + \vec{f} = 0, \tag{47}$$

where $\widetilde{\sigma}$ is the effective stress, $\vec{f}$ is the body force per unit volume and $\widetilde{I}$ is the identity matrix (Wang, 2000, Eq. 4.10). Assuming linear elastic deformation, the stress reads

$$\widetilde{\sigma} = \widetilde{C} : \nabla^s \vec{u}, \tag{48}$$

where $\widetilde{C}$ is the elasticity tensor (Wang, 2000, Eq. 2.42).

The sEFVM determines a nonzero value for the fault slip whenever the Coulomb stresses on a fault node become positive. Further details on the governing equations and initial and boundary conditions are described in Shokrollahzadeh Behbahani et al. (2022).

The computational domain of the sEFVM is shown in Fig. 13. It shows the control volumes for mechanics (Ω_u) and flow (Ω_p) for the matrix. Faults are represented in an embedded manner with unknowns (slip and fault pressure) placed at the location of the fault. In the sEFVM, a jump is appended to the estimation of the displacement field inside a matrix grid (Simo et al., 1993) . The displacement reads

$$\vec{u} \approx \sum_{i=1}^{4} N_i \vec{u}_i + \sum_{i=1}^{n_s} s_i W_i \vec{t}_i, \tag{49}$$

where N are basis functions that interpolate displacement within the cartesian control volume of Fig. 13. For cells intersected by faults, the latter term in Eq. (49) is included. It contains the directional component of the unit tangent vector to the fault ($\vec{t}$). W is defined as

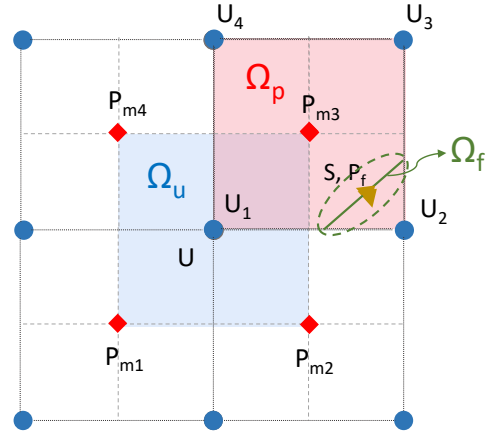$$W(x, y) = \sum_{i=1}^{4} N_i(x, y) \left[H\big(f(x, y)\big) - H\big(f(x_i, y_i)\big) \right], \tag{50}$$

Fig. 13: Representation of the control volumes for the sEFMV method

Table 2: The cell size of adaptive grids shown in Fig. 14 used in calculations.

Case	Boundary cell size, m	Refined cell size, m
without fault	50	20
with fault	100	2

where $f(x, y)$ is the signed distance to the fault and H is a modified Heaviside function defined as

$$H(\zeta) = \begin{cases} -1 & \zeta \leq 0 \\ +1 & \zeta > 0 \end{cases}. \tag{51}$$

The sFVM method numerically solves the momentum balance for the matrix, the friction law for the faults, and the mass balance equations for matrix and faults in a fully-implicit fully-coupled manner.

APPENDIX C. GRIDS USED IN CALCULATIONS

DFM implies a computational grid to be conformal with faults. We use unstructured triangular grids shown in Fig. 14. Grid refinement helps to resolve discontinuities along the fault. characteristic grid sizes used in calculations are listed in Table. 2. sEFVM uses a Cartesian grid for the matrix and the fault is embedded over it as shown in Fig. 15. All sEFVM runs were performed for cell size of 8.3m

APPENDIX D. SEMI-ANALYTICAL TECHNIQUES

Details of the semi-analytical techniques used to generate the results in this paper have been reported in Jansen et al. (2019) and Jansen and Meulenbroek (2022). Here we give a brief overview of these methods
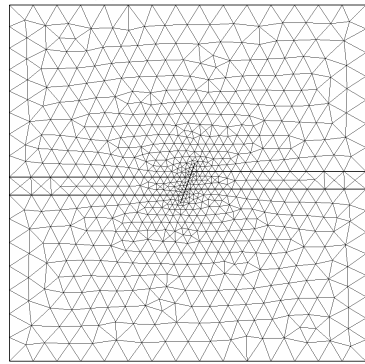
D.1 Inclusion Theory
Linear elastic displacements, strains and stresses inside and outside a reservoir undergoing injection or production
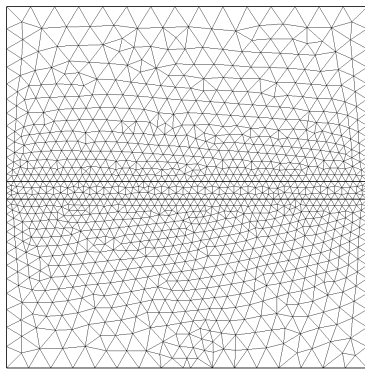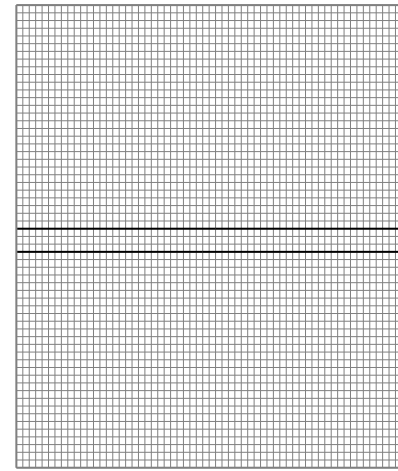
(a) No fault
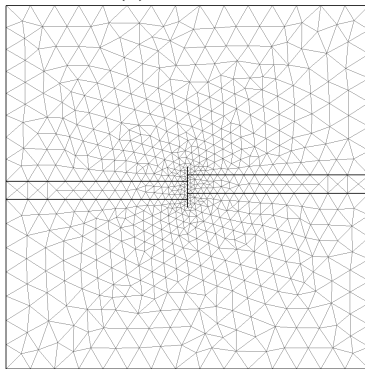
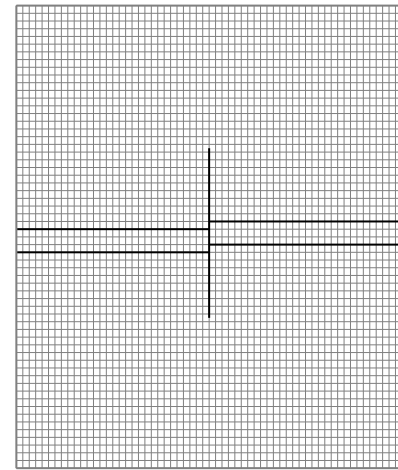(b) Vertical fault

(c) Inclined fault

Fig. 14: Collocated FV with DFM (DARTS) uses adaptive triangular grids illustrated above. The grid size is scaled for convenient representation, the real grid size is listed in Table 2. In the initial stage, the grid is adaptively refined towards the reservoir, in the presence of a fault - towards the fault.

(a) No fault

(b) Vertical fault

(c) Inclined fault

Fig. 15: sEFVM uses cartesian grids with embedded faults. The grid size is scaled for convenient representation, the real grid size is listed in Table 2

can be determined with the 'theory of inclusions' as introduced by Eshelby (1957). Inclusion theory is closely related to the 'nucleus-of-strain' concept (Love, 1927) as discussed in detail by Rudnicki (2002); see also Mura (1987). Inclusion theory and the nucleus of strain concept have been applied to compute stress fields around producing reservoirs to establish the risk on reactivation of nearby (nondisplaced) faults (Segall, 1985, 1989; Segall and Fitzgerald, 1998; Soltanzadeh and Hawkes, 2008).

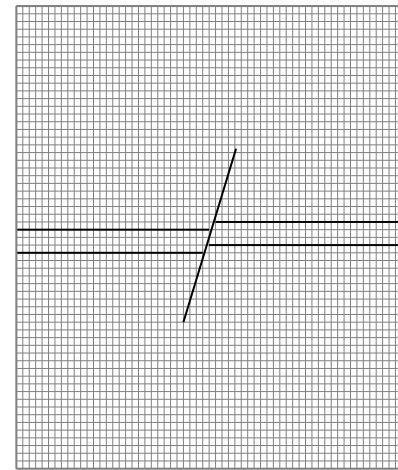Consider a homogeneous porous and permeable inclusion undergoing an increase of pore pressure inside a homo-

geneous infinite domain with the same elastic properties as the inclusion. Flow to or from the outer domain is not possible. An increase in pore pressure in the inclusion

causes a reduction in effective stress in its matrix and consequently an elastic expansion of the inclusion. Fig. 16 depicts a series of imaginary steps that allow for computing the displacements in and around the expanding inclusion as first described by Eshelby (1957):

1) Isolate the inclusion from its surroundings.

2) Allow the inclusion to expand freely.

3) Restore the inclusion to its original shape by applying distributed forces at its boundaries.

4) Re-attach the inclusion to its surroundings and remove the forces, i.e. apply the forces in opposite direction to the entire infinite solid.

The strains resulting from step 2) are known as 'eigenstrains'; they have a finite value inside the inclusion, are zero outside it. The strains resulting from step 4) are called the 'elastic strains' or 'poroelastic strains'; they have a finite value in the entire domain. To achieve step 4), use is made of Greens functions that define the shear and normal strains in any point of the domain as a result of a unit normal force in a point at the boundary. The elastic strain field can then be obtained in the form of a line integral along the boundary. The total strains follow from the superposition of the eigenstrains and the elastic strains. The corresponding stresses can be computed using Hooke's law.
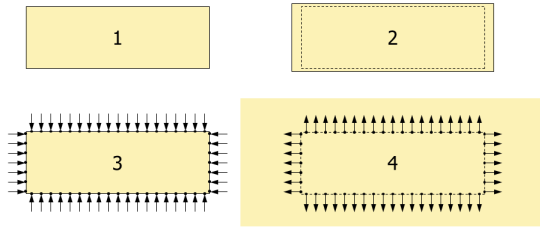

Fig. 16: Imaginary steps involved in computing the displacements in and around an expanding inclusion in an infinite solid.

Jansen et al. (2019) used this method to derive closed-form expressions for the depletion-induced or injection-induced stresses in an inclined displaced fault, i.e. a fault with a nonzero offset. Similar expressions were published concurrently by Lehner (2019) and later by Wu et al. (2021).

D.2 Cauchy Integrals and Chebyshev Polynomials
Inclusion theory (or, alternatively, numerical techniques) can be used to compute the pre-slip Coulomb stress in a fault, defined as

$$\Sigma_C = \Sigma_\| - \Sigma_{sl}$$
$$= \Sigma_\| + \mu \Sigma'_\perp, \tag{52}$$

where $\Sigma_\|$ is the shear stress, Σ_{sl} the slip threshold, $\Sigma'_\perp$ the effective normal stress and μ the friction coefficient.

Note that we use a sign convention where positive stresses correspond to tension.

The sharp 'internal' and 'external' reservoir-fault corners in the reservoir models displayed in Figs. 5 and 7 result in positive-valued peaks in the pre-slip Coulomb stress at $y = \pm a$ and negative-valued peaks at $y = \pm b$, see Figs. 6 and 8. These peaks are, mathematically, of infinite magnitude. In reality, physical effects such as more rounded corners, a finite fault width and pore pressure diffusion between the reservoir and the surrounding rock will somewhat smoothen the stress profile. However, peaks in the pre-slip Coulomb stress profile remain a typical characteristic of displaced faults that experience depletion or injection where it should be noted that as opposed to the peak configuration during depletion, injection results in positive peaks at the external corners and negative peaks at the internal ones (Jansen et al., 2019).

In areas where the pre-slip Coulomb stress is positive, fault slip will occur. However, once slip occurs the stress field in and around the fault changes. In particular, slip-induced shear stresses in the fault occur, which can be shown to have magnitude (Bilby and Eshelby, 1968)

$$\check{\sigma}_\|(y) = -\Sigma_C(y) = A \int_{-\infty}^{\infty} \frac{\nabla \delta(\xi)}{\xi - y} \, d\xi$$
$$= A \left(\int_{\tilde{y}_1}^{\tilde{y}_2} \frac{\nabla \delta(\xi)}{\xi - y} \, d\xi + \int_{\tilde{y}_3}^{\tilde{y}_4} \frac{\nabla \delta(\xi)}{\xi - y} \, d\xi \right), \tag{53}$$

where, for plane-strain conditions,

$$A = \frac{G}{2\pi(1 - \nu)}, \tag{54}$$

with G representing the shear modulus and ν Poisson's ratio, and

$$\nabla \delta(\xi) = \left. \frac{\partial \delta(y)}{\partial y} \right|_{y=\xi}, \tag{55}$$

with δ representing the slip and $\nabla \delta(y)$ the slip gradient along the fault. The variables $\tilde{y}_i, i = 1, ..., 4$, in equation (53) are horizontal projections on the y axis of the lower and upper slip patch boundaries.

The integrands in equation (53) become singular when $\xi = y$. The integrals are therefore Cauchy-type singular integrals which implies that they have to be interpreted in a principal value sense.

For a known pre-slip Coulomb stress distribution Σ_C, both the slip gradient $\nabla \delta(y)$ and the patch boundaries $\tilde{y}_i$ are unknowns that have to be determined from the inverse of equation (53) and additional conditions. Muskhelishvili

(1953) proved that an analytical inversion of singular integral equations can be obtained provided the known function in the integrand is Hölder continuous, which is a stricter form of continuity than regular continuity as applied in mathematical analysis. The closed-form expressions for induced pre-slip Coulomb stresses in a displaced fault contain jump discontinuities at coordinate values $y = \{-b, -a, a, b\}$ in addition to singularities in the form of infinite stress peaks. The jump discontinuities clearly violate the regular and Hölder continuity conditions. An effective way to overcome this difficulty is to regularize the expressions for the shear and normal stresses in the fault, an approach that was followed by Jansen and Meulenbroek (2022).

Cauchy integrals and their corresponding inverse expressions can often be manipulated efficiently with the aid of Chebyshev polynomials (Mason and Handscomb, 2003). Applications in aerodynamics, contact mechanics and fracture mechanics involve both semi-analytical approaches, and numerical methods that strongly rely on the underlying analytical properties of Chebyshev polynomials. Semi-analytical solutions have been applied to model fault slip by Uenishi and Rice (2003), Segall (2010), Van Wees et al. (2019) and Jansen and Meulenbroek (2022).

Using these semi-analytical techniques the development of fault slip can be determined as a function of increasing injection or depletion. Fault slip, which initiates around the peaks in the pre-slip Coulomb stresses, may trigger seismicity in a critically stressed fault, but may also be aseismic, a situation corresponding to the patch growth in Fig. 12. Depending on the friction characteristics of the fault, continuing depletion may result in a gradual aseismic growth of the two slip patches possibly leading to merging. Alternatively, increasing depletion may lead to an unstable situation resulting in a seismic event, see, e.g. Van den Bogert (2015, 2018); Buijze et al. (2017, 2019) and Van Wees et al. (2017) who performed numerical studies into depletion-induced seismicity in displaced faults. A detailed semi-analytical treatment of this phenomenon was reported by Jansen and Meulenbroek (2022).

The semi-analytical benchmark data used to generate the figures in this paper are available in the form of an Excel file uploaded to the 4TU Data Repository with DOI 10.4121/22240309.

REFERENCES

1. Bilby, B. and Eshelby, J. (1968). *Dislocations and the theory of fracture*, volume 1, pages 99–182. Academic Press.

2. Boon, W. and Nordbotten, J. (2022). Mixed-dimensional poromechanical models of fractured porous media. *Acta Mechanica*.

3. Buijze, A., Van den Bogert, P., Wassing, B., and Orlic, B. (2019). Nucleation and arrest of dynamic rupture induced by reservoir depletion. *Journal of Geophysical Research: Solid Earth*, 124:3620–3645.

4. Buijze, A., Van den Bogert, P., Wassing, B., Orlic, B., and Ten Veen, J. (2017). Fault reactivation mechanisms and dynamic rupture modelling of production-induced seismic events in a Rotliegend gas reservoir. *Netherlands Journal of Geosciences*, 96:S131–S148.

5. Cardiff, P., Tukovic, Z., Jaeger, P. D., Clancy, M., and Ivankovic, A. (2017). A lagrangian cell-centred finite volume method for metal forming simulation. *International Journal for Numerical Methods in Engineering*, 109(13):1777–1803.

6. Coussy, O. (2004). *Poromechanics*. Wiley, 2nd ed edition.

7. Eshelby, J. D. (1957). The determination of the elastic field of an ellipsoidal inclusion and related problems. *Proceedings of the Royal Society of London, Series A*, 241:376–396.

8. Hajibeygi, H., Karvounis, D., and Jenny, P. (2011). A hierarchical fracture model for the iterative multiscale finite volume method. *Journal of Computational Physics*, 230(24):8729–8743.

9. Jansen, J. and Meulenbroek, B. (2022). Induced aseismic slip and the onset of seismicity in displaced faults. *Netherlands Journal of Geosciences*, 101(e13).

10. Jansen, J., Singhal, P., and Vossepoel, F. (2019). Insights from closed-form expressions for injection- and production-induced stresses in displaced faults. *Journal of Geophysical Research: Solid Earth*, 124:7193–7212.

11. Lehner, F. (2019). An analysis of depletion-induced fault stressing - new closed-form analytical solutions. Technical report, Nederlandse Aardolie Maatschappij.

12. Li, L., Lee, S. H., et al. (2008). Efficient field-scale simulation of black oil in a naturally fractured reservoir through discrete fracture networks and homogenized media. *SPE Reservoir Evaluation & Engineering*, 11(04):750–758.

13. Li, T., Han, D., Yang, F., Yu, B., Sun, D., and Wei, J. (2020). A comparative study on simulating flow-induced fracture deformation in subsurface media by means of extended fem and fvm. *Oil & Gas Science and Technology-Revue IFP Energies nouvelles*, 75:41.

14. Love, A. (1927). *A Treatise on the Mathematical Theory of Elasticity, 4th ed.* Cambridge University Press. Reprinted in 1944 by Dover.

15. Mason, J. and Handscomb, D. (2003). *Chebyshev Polynomials*. Chapman and Hall.

16. McClure, M. W. and Horne, R. N. (2011). Investigation of injection-induced seismicity using a coupled fluid flow and rate/state friction model. *Geophysics*, 76(6):WC181–WC198.

17. Mura, T. (1987). *Micromechanics of defects in solids, 2nd ed.* Martinus Nijhoff Publishers, Dordrecht.

18. Muskhelishvili, N. (1953). *Singular Integral Equations*. Wolters-Noordhoff, Groningen.

19. Novikov, A., Voskov, D., Hajibeygi, H., and Jansen, J. (2022a). Collocated finite volume scheme for scalable simulation of induced seismicity. *18th European Conference on the Mathematics of Oil Recovery, ECMOR 2022*, (1):1–18.

20. Novikov, A., Voskov, D., Khait, M., Hajibeygi, H., and Jansen, J. (2022b). A scalable collocated finite volume scheme for simulation of induced fault slip. *Journal of Computational Physics*, 469:111598.

21. NWO (2017). DeepNL Research Programme.

22. Rudnicki, J. (2002). Elsheby transformations, pore pressure and fluid mass changes, and subsidence. In *Poromechanics II, 2nd Biot Conf. Poromech.* Aug. 26-28, Grenoble, France.

23. Segall, P. (1985). Stress and subsidence resulting from subsurface fluid withdrawal in the epicentral region of the 1983 Coalinga earthquake. *Journal of Geophysical Research*, 90:6801–6816.

24. Segall, P. (1989). Earthquakes triggered by fluid extraction. *Geology*, 17:942–946.

25. Segall, P. (2010). *Earthquake and Volcano Deformation*. Princeton University Press.

26. Segall, P. and Fitzgerald, S. (1998). A note on induced stress changes in hydrocarbon reservoirs and geothermal reservoirs. *Tectonophysics*, 289:117–128.

27. Shokrollahzadeh Behbahani, S., Hajibeygi, H., Voskov, D., and Jansen, J. (2022). Smoothed embedded finite-volume method (sEFVM) for modeling contact mechanics in deformable faulted and fractured porous media. *Journal of Computational Physics*.

28. Simo, J. and Laursen, T. (1992). An augmented lagrangian treatment of contact problems involving friction. *Computers and Structures*, 42(1):97–116.

29. Simo, J. C., Oliver, J., and Armero, F. (1993). An analysis of strong discontinuities induced by strain-softening in rate-independent inelastic solids. *Computational Mechanics*, 12(5):277–296.

30. Soltanzadeh, H. and Hawkes, C. (2008). Semi-analytical models for stress change and fault reactivation induced by reservoir production and injection. *Journal of Petroleum Science and Engineering*, 60:71–85.

31. Uenishi, K. and Rice, J. (2003). Universal nucleation length for slip-weakening rupture instability under nonuniform loading. *Journal of Geophysical Research: Solid Earth*, 108:ESE 17–1 17–14.

32. Van den Bogert, P. (2015). Impact of various modelling options on the onset of fault slip and fault slip response using 2-dimensional finite-element modelling.

33. Van den Bogert, P. (2018). Depletion-induced fault slip and seismic rupture: 2D geomechanical models for the Groningen field, the Netherlands.

34. Van Wees, J., Fokker, P., Van Thienen-Visser, K., Wassing, B., Osinga, S., Orlic, B., Ghouri, S., Buijze, L., and Pluymaekers, M. (2017). Geomechanical models for induced seismicity in the Netherlands: inferences from simplified analytical, finite element and rupture model approaches. *Netherlands Journal of Geosciences*, 96:S183–S202.

35. Van Wees, J., Pluymaekers, M., Osinga, S., Fokker, P., Van Thienen-Visser, K., Orlic, B., Wassing, B., Hegen, D., and Candela, T. (2019). 3-d mechanical analysis of complex reservoirs: a novel mesh-free approach. *Geophysical Journal International*, 219:1118–1130.

36. Wang, H. (2000). *Theory of linear poroelasticity with applications to geomechanics and hydrogeology*. Princeton University Press.

37. Wu, H., Vilarrasa, V., De Simone, S., Saaltink, M., and Parisio, F. (2021). Analytical solution to assess the induced seismicity potential of faults in pressurized and depleted reservoirs. *Journal of Geophysical Research: Solid Earth*, 126:e2020JB020436.

38. Xu, F., Hajibeygi, H., and Sluys, L. J. (2021). Multiscale extended finite element method for deformable fractured porous media. *Journal of Computational Physics*, 436:110287.

39. Yastrebov, V. A. (2013). *Numerical Methods in Contact Mechanics*. ISTE. Wiley-ISTE, 1 edition.